Masoud Rostami and Vladimir Zeitlin

ARTICLES YOU MAY BE INTERESTED IN

Evolution of double-eye wall hurricanes and emergence of complex tripolar end states in moist-convective rotating shallow water model

View Online   Export Citation   CrossMark

Masoud Rostami[1] (iD) and Vladimir Zeitlin[2,a] (iD)

AFFILIATIONS

[1]Earth System Analysis, Potsdam Institute for Climate Impact Research (PIK), Member of the Leibniz Association, Potsdam, Germany
[2]Laboratory of Dynamical Meteorology, Sorbonne University, Ecole Normale Supérieure, CNRS, 24 rue Lhomond, 75005 Paris, France

[a]Author to whom correspondence should be addressed: zeitlin@lmd.ens.fr

ABSTRACT

A detailed investigation of linear instabilities of double-eyewall hurricane-like vortices with double maxima ("walls") of azimuthal velocity and vorticity around the central minimum ("eye") and of their nonlinear saturation is carried out in the framework of the moist-convective rotating shallow water model. It is shown that developing barotropic instability leads to inward displacement and gradual disappearance of the inner wall and to the formation of a nontrivial tripolar quasi-stationary structure, provided the second, outer, wall of the initial vortex is high enough. The effects of moist convection lead to the enhancement of the outer wall. In comparison, under the influence of the same instability, vortices with an inner wall stronger than the outer one evolve toward monopolar single-eyewall structures.

Published under an exclusive license by AIP Publishing. https://doi.org/10.1063/5.0096554

I. INTRODUCTION

From a hydrodynamical viewpoint, the horizontal structure of a typical hurricane is characterized by a low vorticity zone at the center, which is associated with the hurricane's eye, surrounded by a high vorticity ring, which is associated with the eyewall. However, there is a bulk of observational evidence of double-eyewall hurricanes, and the formation of a secondary eyewall during the evolution of the inner core structure of hurricanes is not an uncommon event, particularly in intense, highly symmetric systems.[1,2] Satellite-based microwave imagers confirm the existence of secondary eyewalls.[3] For example, roughly concentric rings have been observed in the satellite microwave images of hurricane Frances on 30 September 2004, and hurricane Katrina on 28 August 2005.[4] Analogously to the primary eyewall, secondary wind maxima are often coupled with a convective ring.[5] A process of eyewall replacement, called eyewall replacement cycle (ERC) or a concentric eyewall cycle, is described in the literature[1,6,7] and consists of contraction, or inward shift, of the primary eyewall during the storm intensification and replacement of the primary eyewall by the second one, once the secondary eyewall is enough grown. The replacement leads to weakening and eventual disappearance of the inner wall, while the secondary eyewall gets amplified to the strength of the primary eyewall, during the ERC as seen in the wind maximum, and

vorticity and convection fields. The word "cycle" in this context refers to repetitive scenarios of contraction and replacement of the inner eyewall. The contraction of the eyewall is ascribed to a ring of convection inside the radius of maximum heating that causes an inward shift.[8,9] By analyzing 31 years of flight-level data, Sitkowski *et al.*[10] exhibited 24 ERC events in 14 hurricanes. Although the ERC is well documented, dynamical processes in double-wall vortices with a "moat" between the walls are not sufficiently understood.

The rotating shallow water (RSW) model, with or without the inclusion of diabatic effects, proved to be a simple and reliable tool for understanding the basics of hurricanes' dynamics, see the recent papers[11–15] and references for a bulk of earlier work therein. Recently, this model was applied to double-eyewall tropical cyclone (TC) like vortices[16] in order to understand the interactions of the two walls across the moat, which are produced by the instabilities of such configurations. Motivated by this work, we go further in the same direction by performing a detailed linear stability analysis of the double-eyewall TC-like vortices and by using a consistent inclusion of dynamical effects of moisture, offered by the so-called moist-convective RSW (mcRSW),[17,18] for fully nonlinear high-resolution numerical simulations of the nonlinear development of the instabilities. We, thus, identify the most unstable modes of the intense double-wall vortices, study

their dependence on the relative height of the walls, and investigate nonlinear saturation of the instability both in "dry" and moist-convective settings, in order to understand the influence of moisture upon this process. Our main finding is a robust tripolar vortex structure arising at the late stages of the evolution of double-wall TC-like vortices with comparable heights of the walls.

II. THE MODEL AND THE VORTEX CONFIGURATION
A. A reminder on mcRSW model

We use the simplest one-layer version of the mcRSW model proposed in Ref. 17, with an addition of a source of moisture representing evaporation, as described in Refs. 11 and 19. No explicit dissipation of any kind is included in the model. The equations of the model are

$$\begin{cases} \partial_t \mathbf{v} + \mathbf{v} \cdot \nabla \mathbf{v} + f \hat{\mathbf{z}} \wedge \mathbf{v} = -g\nabla h, \\ \partial_t h + \nabla \cdot (\mathbf{v} h) = -\gamma C, \\ \partial_t Q + \nabla \cdot (Q\mathbf{v}) = -C + E. \end{cases} \quad (1)$$

Here, x and y are the zonal and meridional coordinates on the tangent plane, $\nabla = (\partial_x, \partial_y)$ and $\mathbf{v} = (u, v)$, respectively, u and v are the zonal and meridional components of velocity, respectively, h is the geopotential height (thickness), f is the Coriolis parameter, which is taken to be constant $f = f_0$ as we are working in the f-plane approximation, and $\hat{\mathbf{z}}$ is the unit vertical vector. $Q \geq 0$ is specific humidity integrated over the air column, γ is a parameter depending on the underlying stratification, C is the condensation sink, and E is the surface evaporation source of moisture. They are parameterized as follows, and in the dry version of the model, they are simply set to zero,

$$C = \frac{Q - Q^s}{\tau} \mathcal{H}(Q - Q^s), \quad E = \alpha \frac{|\mathbf{v}|}{|\mathbf{v}_{\max}|} (Q^s - Q)\mathcal{H}(Q^s - Q). \quad (2)$$

Here, Q^s is a saturation threshold, which we consider to be pressure-dependent, as explained in Ref. 17, see below. In principle, the evaporation threshold could be chosen to be different from Q^s, as the evaporation, physically, does not take place through the whole air column. We take it to be the same in the crudest variant of the model, in order to avoid the proliferation of free parameters. τ is the relaxation time, which is of the order of several hours in the tropical atmosphere. The parameterization of evaporation in (2) is based on the standard bulk formula, cf., e.g., Ref. 20, which is of frequent use in hurricane modeling,[21] where we renormalized the transmission coefficient by $|\mathbf{v}_{\max}|$, the maximum value of velocity over the domain, i.e., the maximum wind in the hurricane-like vortices we consider, in order to get the non-dimensional parameter α regulating the intensity of evaporation. This is a free parameter, the only one representing processes in the unresolved boundary layer in the present formulation of the model; its value in the simulations will be given below. $\mathcal{H}(\cdots)$ denotes the Heaviside (step-) function, which accounts for the switch character of condensation and evaporation. As is natural in the context of TC modeling, we consider the vortex motion mostly over the ocean, where the bulk formula for evaporation (2) is well adapted.

B. TC-like vortex configuration

The equations of the model in polar coordinates read

$$\begin{cases} \dfrac{d\mathbf{v}}{dt} + \left(f + \dfrac{v}{r}\right)\hat{\mathbf{z}} \wedge \mathbf{v} + g\nabla h = 0, \\ \partial_t h + \dfrac{1}{r}(\partial_r(rhu) + \partial_\theta(hv)) = -\gamma C, \\ \partial_t Q + \dfrac{1}{r}(\partial_r(rQu) + \partial_\theta(Qv)) = -C + E, \end{cases} \quad (3)$$

where $\mathbf{v} = (u\,\hat{\mathbf{r}}(r, \theta), v\,\hat{\theta})$ is the velocity in polar coordinates, and the Lagrangian derivative is $\frac{d}{dt} = \frac{\partial}{\partial t} + u\partial_r + \frac{v}{r}\partial_\theta$.

In the absence of evaporation, the axisymmetric azimuthal velocity $v(r)$ and thickness $h(r)$ in cyclo-geostrophic equilibrium

$$\frac{v^2}{r} + fv = g\,\partial_r\,h, \quad (4)$$

at zero radial velocity $u = 0$ and arbitrary constant or azimuthally symmetric $Q(r) \leq Q^s$ give an exact solution of (3). In the presence of evaporation, in order to provide an exact solution, Q should stay at the evaporation threshold, i.e., $Q = Q^s$, with the choice of the threshold made above.

In order to construct a double-wall TC-like vortex, we start with the non-dimensional profile of azimuthal velocity $V(r)$, which was already used for single-wall TC in the previous work,[15]

$$\bar{V}(r) = (r - r_0)^a e^{-c(r-r_0)^b}, \quad r > r_0, \, a, b, c > 0. \quad (5)$$

To control the strength of the vortex, we introduce a non-dimensional amplitude ϵ and renormalize $\bar{V}(r)$ as follows:

$$\bar{V}(r) \to V(r) = \varepsilon \frac{\bar{V}(r)}{\max|\bar{V}(r)|}. \quad (6)$$

This "abc" profile is placed at a distance r_0 from the origin and is matched at r_0 with a linear velocity profile in the interval $[0, r_0]$, in a way to reproduce the observed approximately constant-vorticity eye and to have continuous velocity and vorticity. Here, r is the non-dimensional radius from the center of the vortex. We use the following scaling: horizontal distances are measured in units of the barotropic deformation radius, $R_d = \sqrt{gH}/f$, time in units of $1/f$, and velocities are measured in units of $\sqrt{gH}$, where H is the total thickness of the atmospheric column at rest. According to this scaling, the Rossby number Ro is proportional to ε/RMW, where RMW is the non-dimensional radius of maximum wind. The Rossby number in the velocity profile of Fig. 1 is $Ro = 1.67$.

The velocity profile of a double-eye configuration is obtained by superposition of two (a, b, and c) profiles. In the case of comparable heights of the two walls, which is the main configuration under the present study (see Sec. IV for another configuration), the parameters (a, b, and c) are taken to be equal to ($4.5, 0.18$, and 48) for both the inner and outer walls, and (r_0, ε) for the inner and outer walls is ($0.01, 0.06$) and ($0.08, 0.09$), respectively. A particular feature of this background velocity profile, which can be seen in the upper-left panel of Fig. 1, together with the corresponding typical double-wall relative vorticity profile, is its steeper ascent before the radius of maximum wind, and a slower descent out of it, which is in agreement with observed velocity profiles.[22] The corresponding profile of thickness deviation can be found by calculating the primitive of the left-hand side of (4) and is shown in the upper-right panel of Fig. 1.
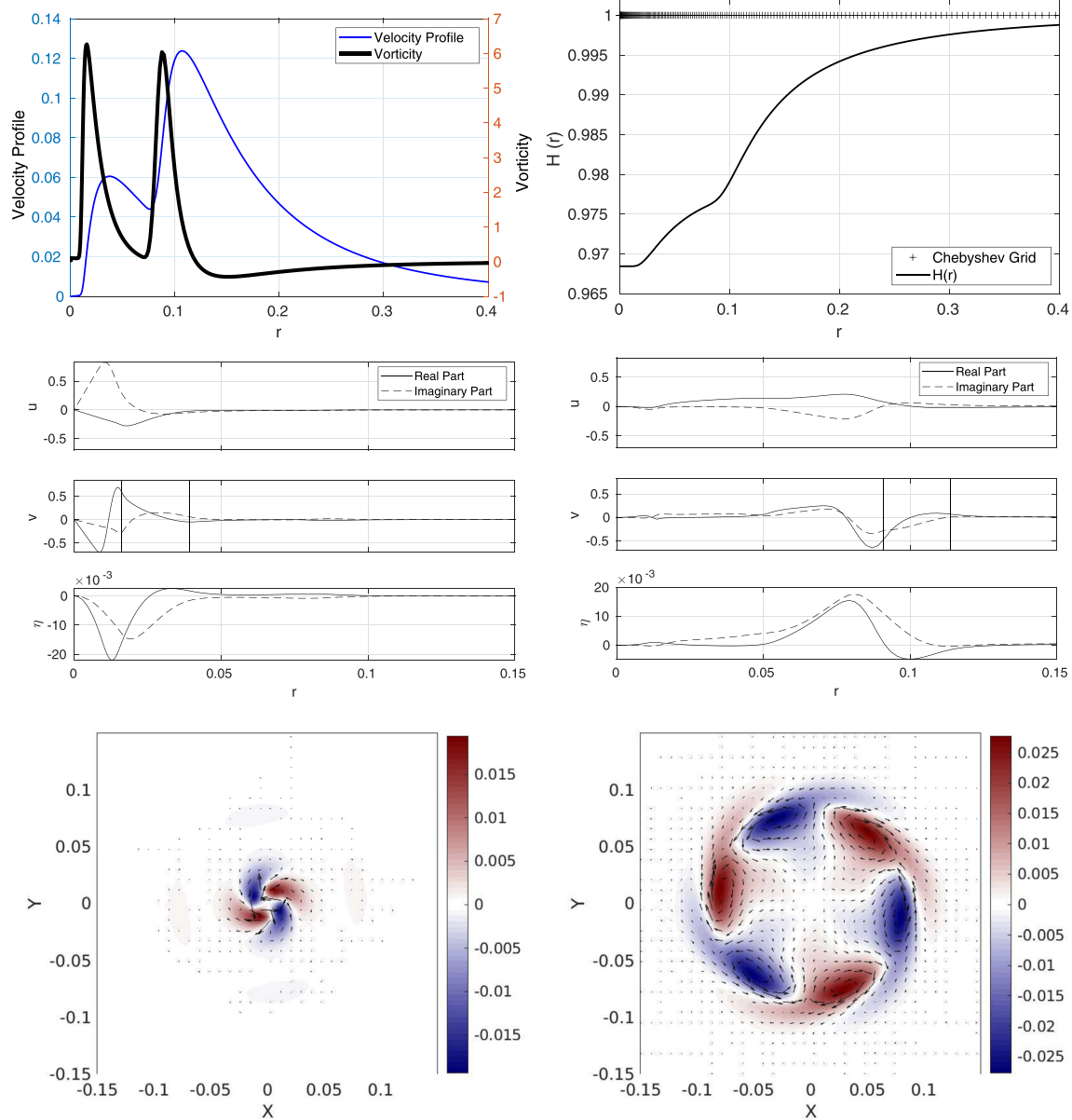
FIG. 1. Upper row: left panel—azimuthal velocity profile and vorticity of the background barotropic double eyewall cyclone. Right panel—Chebyshev grid points and thickness of the vortex $H(r)$. Middle row: radial structure of the velocity and thickness perturbations $(u, v, \eta)(r)$, respectively, corresponding to the unstable modes with $l = 2$ (left panel) and $l = 3$ (right panel). Vertical lines indicate positions of the critical levels. Lower row: the pressure and velocity field of the most unstable mode $l = 2$, left panel, and the second unstable mode $l = 3$, right panel.

III. DYNAMICS OF DOUBLE-EYEWALL TC-LIKE VORTEX WITH COMPARABLE INTENSITY OF VORTICITY PEAKS

A. Results of the linear stability analysis

The linear stability analysis is performed along the lines of similar studies of single-wall TC-like vortex profiles.[11,15] For this, Eq. (3) is linearized about the corresponding profiles of azimuthal velocity and thickness, cf. the upper row of Fig. 1. Solutions of the linearized equations are sought in the form of Fourier-modes in time and polar angle (azimuthal modes with integer wavenumber l), with the radial structure determined by solutions of the resulting eigenproblem for frequencies at a given azimuthal wavenumber. Solutions are obtained numerically after discretization on a Chebyshev grid shown in the upper-right panel of Fig. 1, solving the resulting finite-dimensional matrix eigenproblem.

The lower panel of Fig. 1 displays the phase portraits of the most unstable modes. As follows from the mutual orientation of velocity and isobars, the most unstable modes are close to the geostrophic
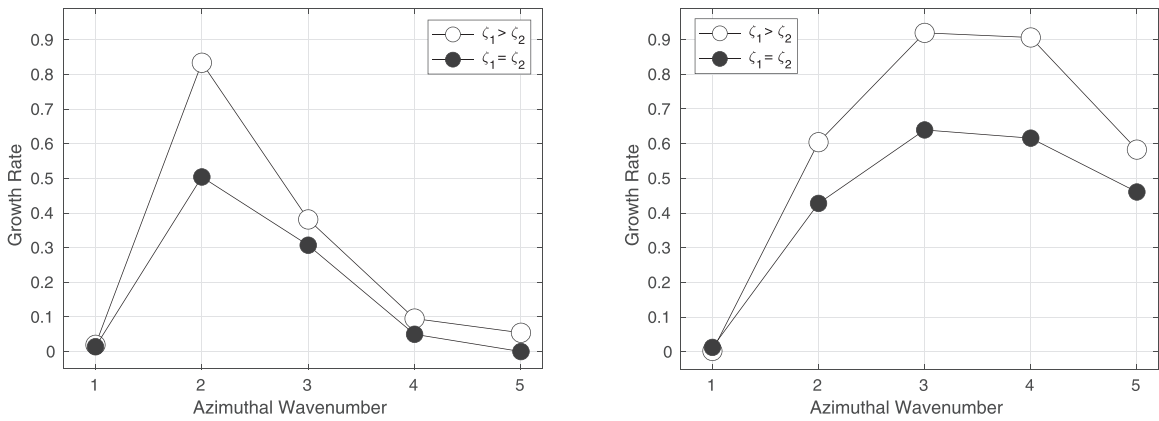
FIG. 2. Left panel: Variations of the growth rate of unstable modes with azimuthal wavenumber for two background configurations with $\zeta_1 \approx \zeta_2$, as in Fig. 1, and with $\zeta_1 > \zeta_2$ presented in Fig. 12 in Sec. IV, where $\zeta_{1,2}$ are the first and second maxima of relative vorticity, respectively. Right panel: Same as in the left panel, but with the radius of maximum wind shifted by $0.02R_d$ farther from the center.
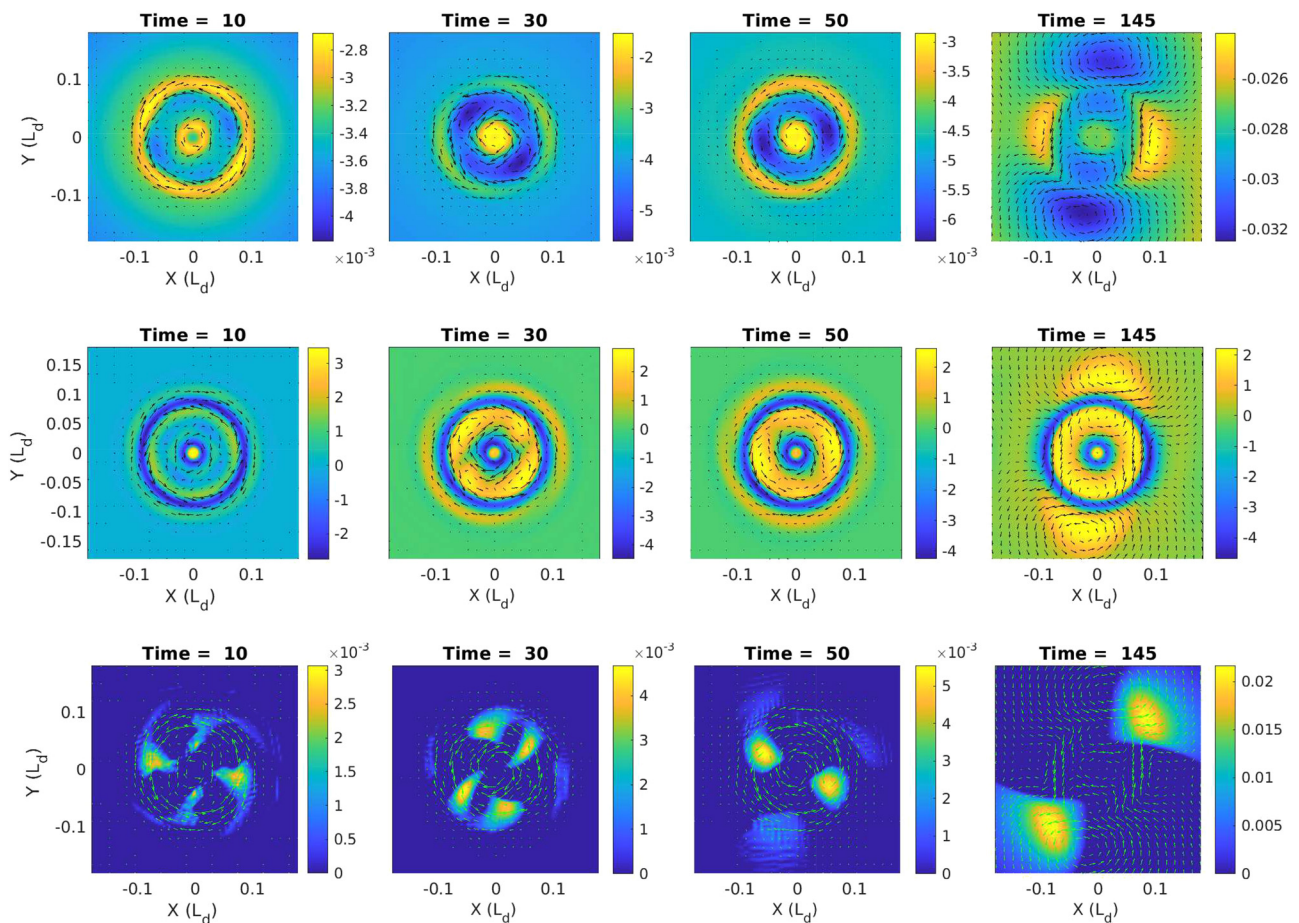

FIG. 3. Evolution of the pressure anomaly, relative vorticity, and condensation of double-eyewall cyclone initialized, as shown in Fig. 1, with the most unstable mode, $l = 2$, in moist-convective environment during the saturation of the barotropic instability, respectively, from top to bottom.

balance, thus being Rossby waves, which are typical for barotropic instability, having azimuthal wavenumbers $l = 2$ and $l = 3$, respectively, and propagating along the inner and outer walls due to background vorticity gradients. The unstable mode with $l = 3$ is located in the vicinity of the outer eyewall, while the unstable mode with $l = 2$ is located at the inner eyewall.

Dependence of the growth rate of the unstable modes on the azimuthal wavenumber for two positions of the radius of maximum wind of the background vortex is presented in Fig. 2. For comparison, we simultaneously present these results for a background vortex with the inner wall significantly more intense than the outer one.

As follows from Fig. 2, at least with the shape of the vortex we use, the azimuthal structure of the most unstable mode is not sensible to the relative intensity of the walls, but its growth rate is. On the contrary, both are sensible to the value and position of the RMW. As the next step, we will use separately the most unstable modes $l = 2$, $l = 3$ for the initialization of fully nonlinear numerical simulations, by superimposing them with the weak amplitude 0.015 onto the background vortex.

B. Nonlinear saturation of the instability

We now present results of direct numerical simulations initialized with the perturbations corresponding, respectively, to the middle- and lower-left and middle- and lower-right panels of Fig. 1 superimposed onto the background vortex configuration of the upper row of Fig. 1. The details of the numerical scheme for mcRSW and its implementation can be found in our previous above-cited works. We should only emphasize that the well-balanced finite-volume quasi non-dissipative method we are using allows for long-time high-resolution simulations representing the saturation of the instability with high fidelity. In the present study, we apply the finite-volume numerical code in the computational domain of the size $L_x = L_y = 1.2 [R_d]$ subdivided into 400×400 grid cells. Neumann boundary conditions are used in order to evacuate the emitted inertial gravity waves. The numerical time step is $10^{-3} [f_0^{-1}]$. All simulations are performed in both dry and moist-convective environments. The main focus of this study is on the double-eyewall configuration with comparable vorticity at each wall as shown in Fig. 1; nevertheless, a summary of results for a configuration with the outer eyewall with weaker vorticity is presented in Sec. IV. Following Bouchut et al.,[17] we choose Q^s as a function
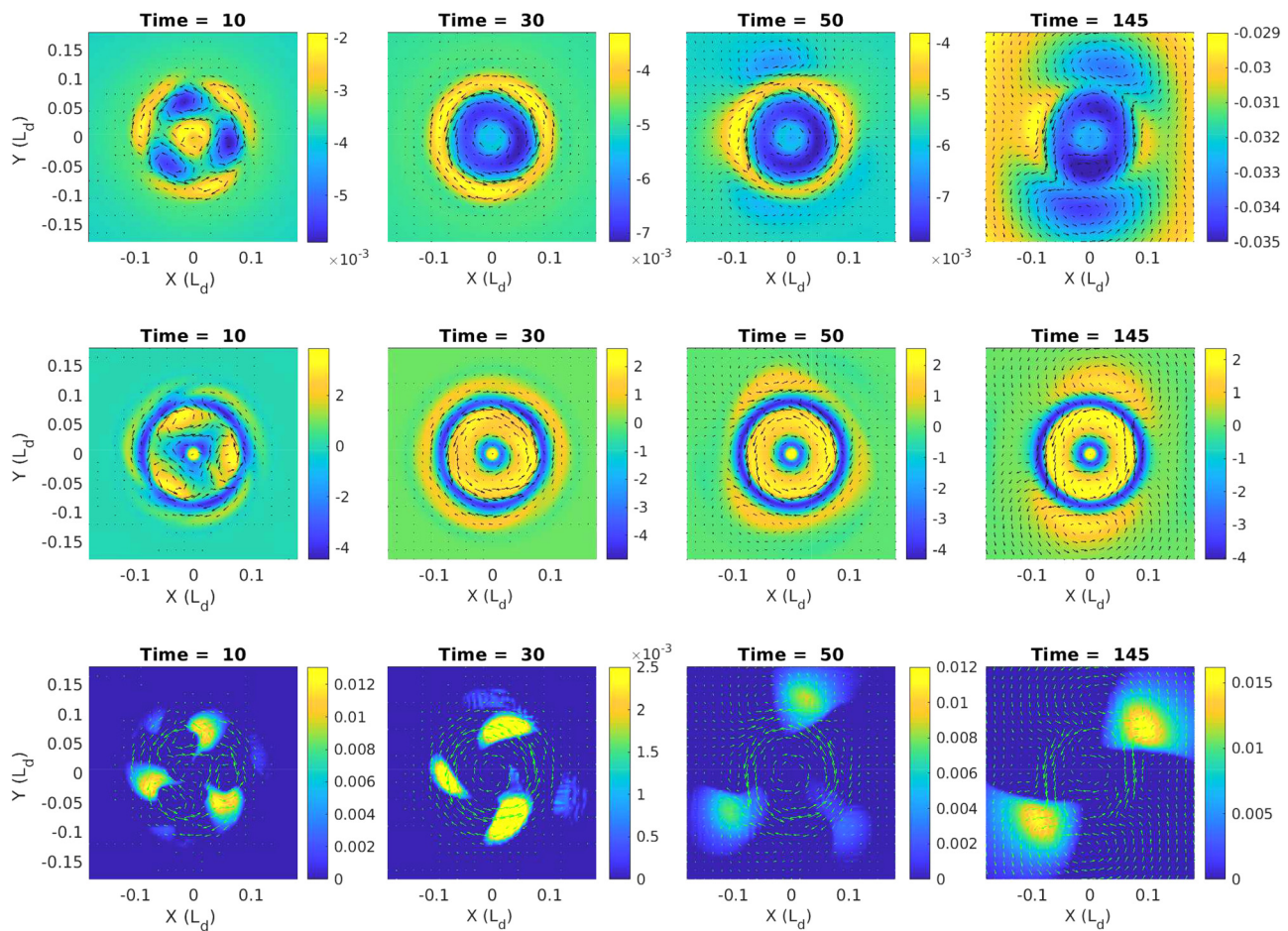

FIG. 4. Same as in Fig. 3, but for initialization with the unstable mode $l = 3$.
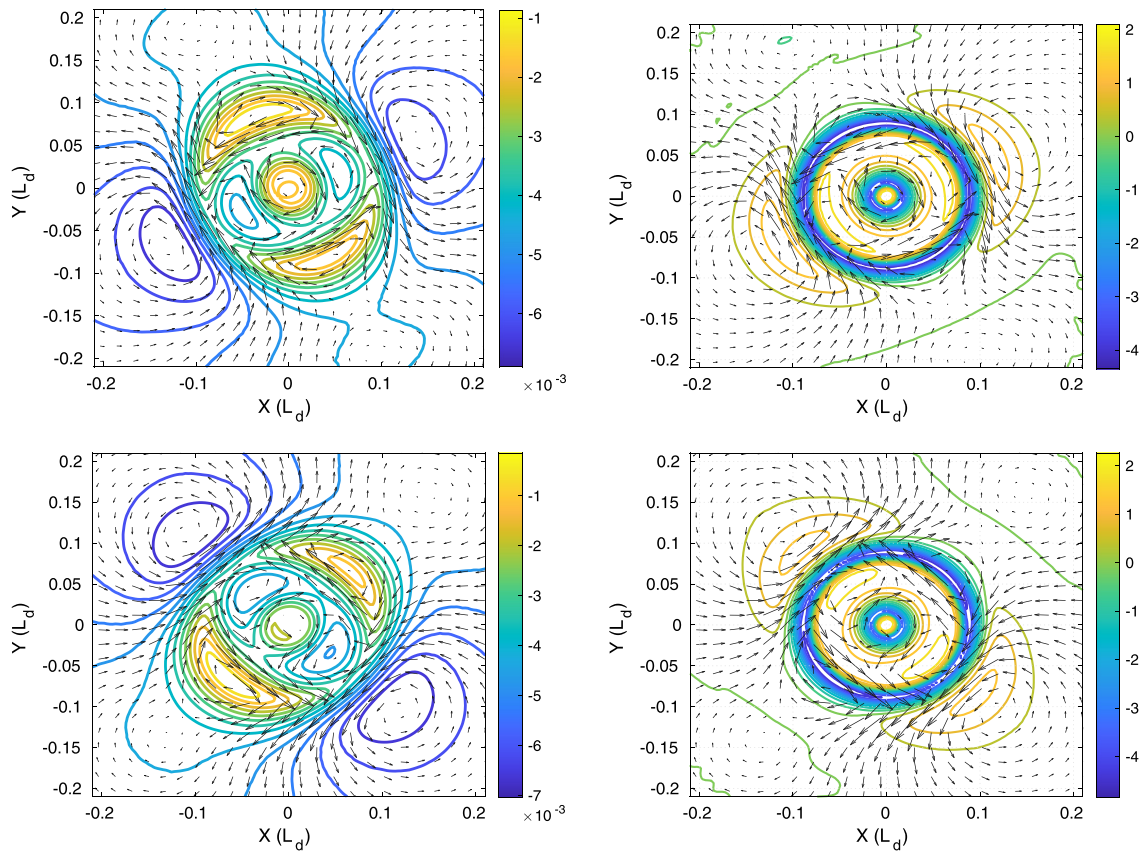
FIG. 5. Late stage of the evolution of pressure anomaly (left column) and relative vorticity (right column) of the double-eyewall cyclone of Fig. 1 in an adiabatic (dry) environment during the saturation of the barotropic instability initialized with a pure unstable mode $l = 2$ (upper row) and $l = 3$ (lower row) at time $T = 175 \, [f_0^{-1}]$.

depending on pressure anomaly. The saturation threshold is taken in the form $Q^s = Q_0 + \alpha'(h - H)$, with $\alpha' = 0.04$, and the initial value of humidity $Q_0 = 0.9$. $H = 1$, α and γ ($\alpha = 0.5$, $\gamma = 0.9$) are constants regulating the intensity of surface evaporation and latent heat

release, respectively. The condensation relaxation time τ is taken to be $0.04 \, [f_0^{-1}]$.

Figure 3 shows the evolution of pressure and relative vorticity of the double-eyewall vortex with equal intensity of the walls with
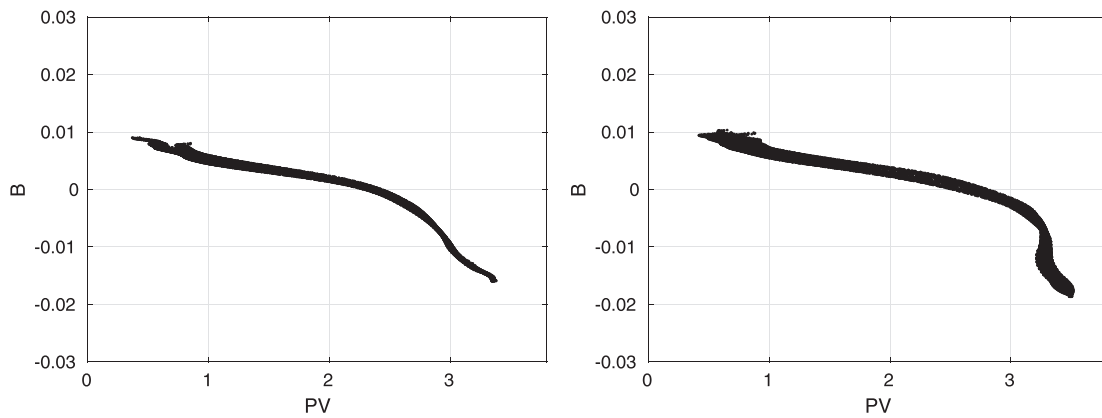

FIG. 6. Scatter plot of the Bernoulli function (with subtracted mean value) vs potential vorticity (PV) in adiabatic (left panel) and moist-convective (right panel) environments (time = $140 [f_0^{-1}]$). Initial conditions as in Fig. 1 with $l = 2$.
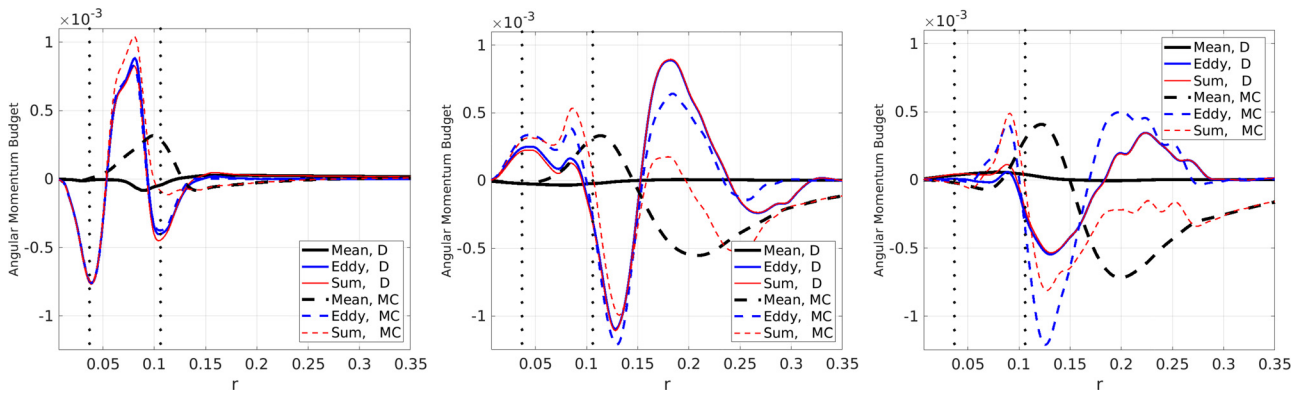
FIG. 7. Contributions to angular momentum of eddy, mean, and total fluxes integrated over three different time spans $\Delta t = [0, 50]$, $[51, 100]$, $[101, 145]$, and $[f_0^{-1}]$, from left to right, during the evolution of double-eyewall vortex with almost equal vorticities of the walls with the superimposed unstable mode $l = 2$, in dry (solid) and moist-convective (dashed) environments. Vertical dots indicate the radial position of the radii of maximum winds of the inner and outer eyewalls at initial time.
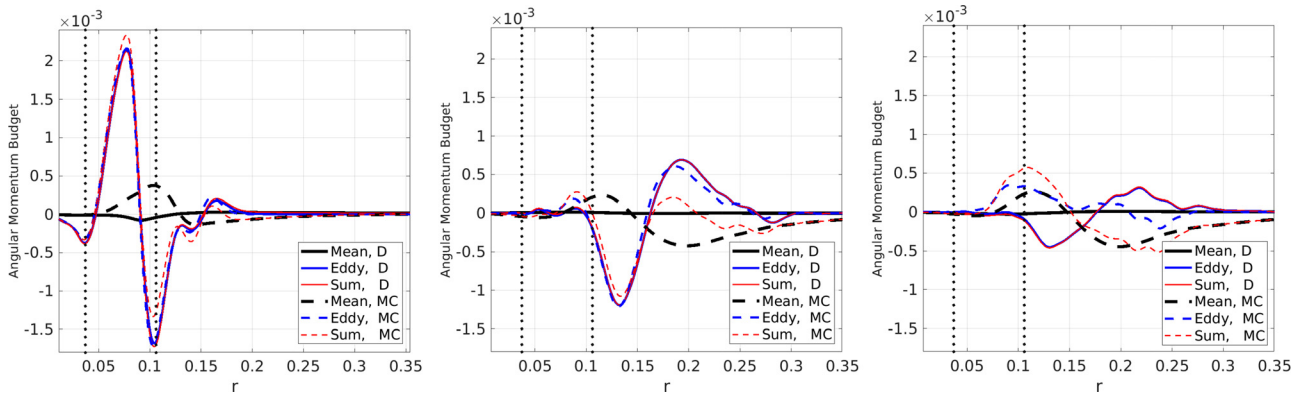

FIG. 8. Same as in Fig. 7, but for initialization with the superimposed unstable mode $l = 3$.
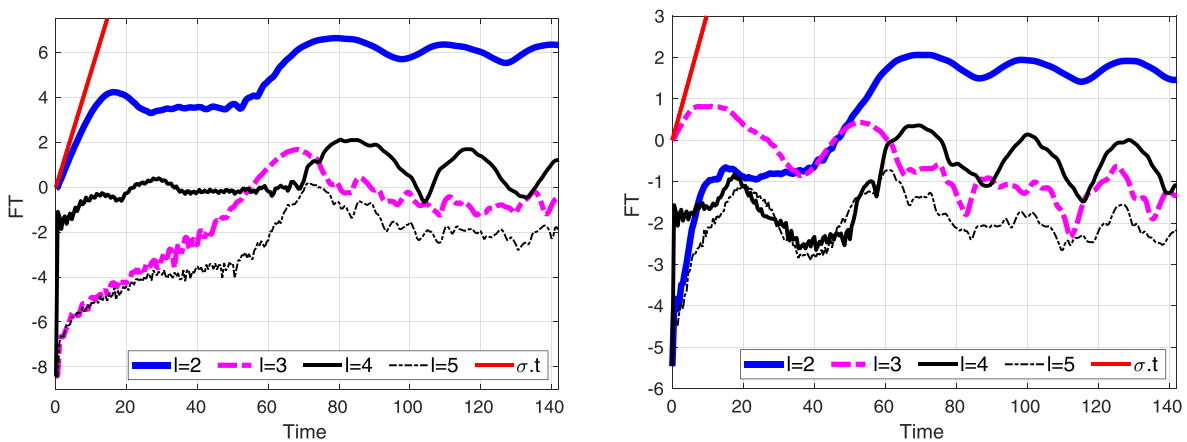
FIG. 9. Logarithms of the normalized amplitudes of the Fourier modes of azimuthal velocity as functions of time during the evolution of the barotropic instability in moist-convective environment in simulations initialized with the most unstable mode $l = 2$ (left panel) and the second unstable mode $l = 3$ (right panel). Initial conditions as in Fig. 1. The red straight line represents the growth rate σ as a function of time, following from linear stability analysis.

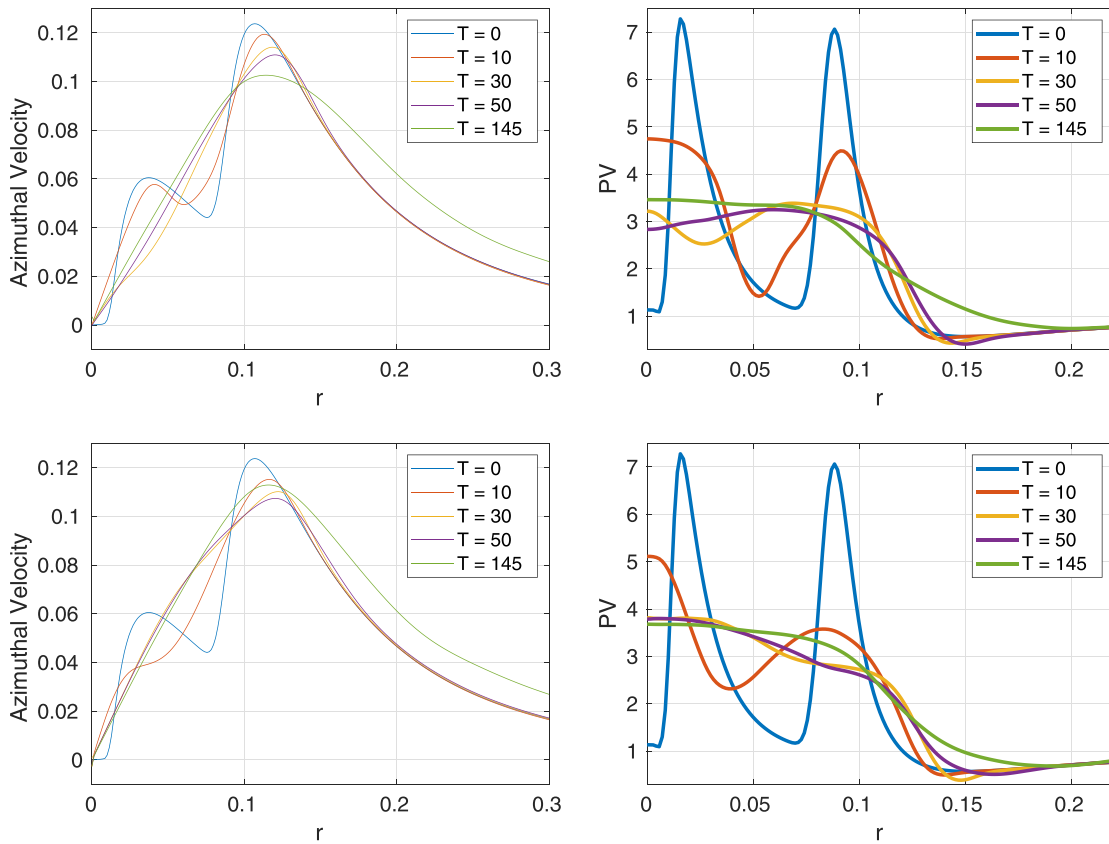**FIG. 10.** Time evolution of radial distributions of azimuthally averaged azimuthal velocity (left panel) and PV (right panel) in moist-convective environment for the simulations initialized with the most unstable mode, $l = 2$ (upper row) and $l = 3$ (lower row).

superimposed unstable mode $l = 2$ in moist-convective environment. As follows from the figure, the outer eyewall considerably influences the evolution of the instability, which is initially located in the vicinity of the inner eyewall. The figure clearly shows the formation of a specific structure at the end stages of evolution, which consists of a single-eyewall central cyclonic vortex surrounded by two rings of anti-cyclonic vorticity and two external cyclonic lobes beyond. This end state further preserves its structure for a long time and thus is not
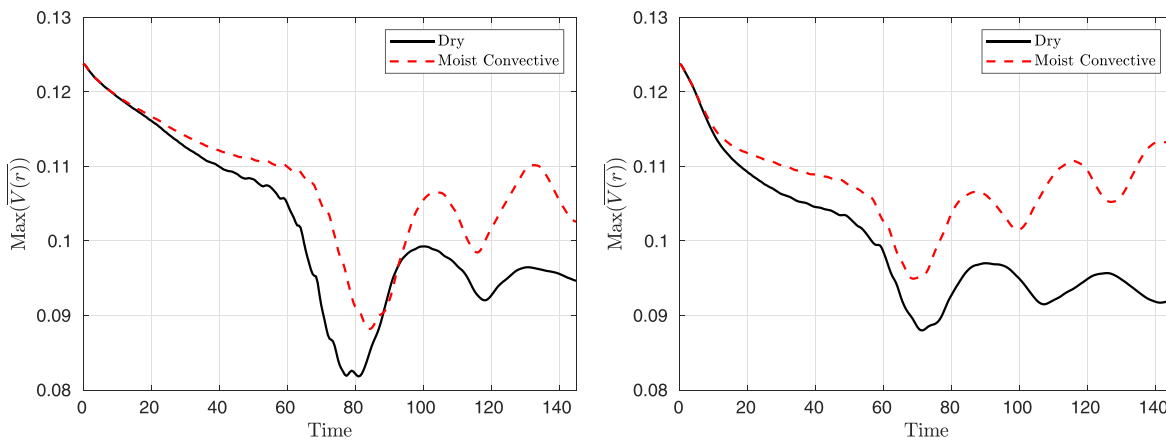

FIG. 11. Comparison of the evolution of the peak values of azimuthally averaged velocity in the adiabatic and moist-convective environments for initial conditions corresponding to Fig. 1 with $l = 2$ (left panel) and $l = 3$ (right panel).

axisymmetric, unlike the end-states of evolution of instabilities of single-eyewall vortices in the same model,[11] and is rotating like a vortex tripole. Simulations with other initializations, e.g., a pure unstable mode with $l = 3$ (Fig. 4), or a combination of modes $l = 2$ and $l = 3$ (not shown) produce the same scenario at the late stages. Such a structure is robust and emerges already in the adiabatic, dry, environment. We show in Fig. 5 the formation of this structure in the simulations initialized with unstable modes $l = 2$ and $l = 3$ in the dry environment. The fact that the evolution does lead to the formation of a coherent structure is confirmed by the scatterplot of the Bernoulli function vs potential vorticity presented in Fig. 6. Such scatter plots are standard in diagnosing coherent structures of any nature in rotating shallow water models, cf. Refs. 23–25 and references therein. The structure in question is coherent if the points of the plot form a curve, as compared to a dispersed cloud in the opposite case. We should stress that the observed endstate, although being tripolar in essence, has a much more complicated form than tripolar vortex solutions known for 2D Euler[26] and rotating shallow water[23] equations, and observed in laboratory experiments,[27] due to essentially non-monotonous and sign-changing distribution of vorticity in the central vortex.

Following Hendricks *et al.*[28] and Lahaye and Zeitlin,[11] we also investigated tangential momentum and absolute angular momentum budgets during the evolution of the aforementioned double-eyewall

configuration. The equation for absolute angular momentum in the absence of dissipation is

$$\frac{\partial \bar{M}}{\partial t} = -\hat{u}\frac{\partial \bar{M}}{\partial r} - r\overline{hq^*u^*}, \tag{7}$$

where $\overline{()}$ indicates the azimuthal average, $\hat{u} = (\overline{hu}/\bar{h})$ is the mass-weighted average of the radial velocity, $\bar{M} = r\bar{v} + (1/2)fr^2$ is the azimuthal-mean absolute angular momentum per unit mass, $u^* = u - \hat{u}$ is the deviation of azimuthal velocity from the mass-weighted average, and $q^* = q - (\overline{hq}/\bar{h})$ is the deviation of potential vorticity from its mass-weighted azimuthal average. The first and second terms on the right-hand side of Eq. (7) correspond to the processes involving the mean and eddy fields, respectively, which will be referred to below as the "mean flux" and the "eddy flux," respectively. Figure 7 displays the contributions to the total angular momentum change due to the eddy and mean fluxes during the three main phases of its evolution: initial stages, transition to the coherent tripolar state, and later stages, in both dry and moist-convective environments. Integration is based on the trapezoidal rule over time spans using the $0.5 \, [f_0^{-1}]$ output data. At the initial stages (left panel of the figure), the eddy flux between two radii of maximum winds is strong and leads to filling in the moat and inward displacement of the outer eyewall, which is clearly seen in the evolution of the mean azimuthal velocity
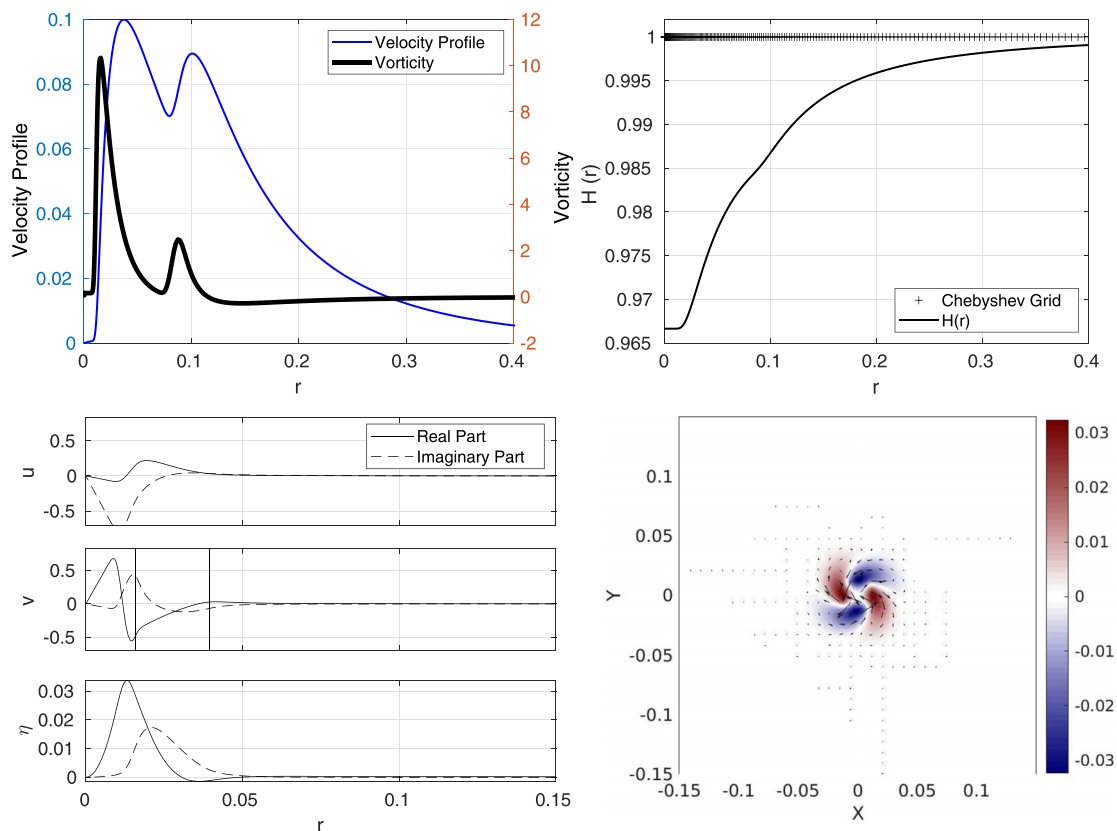
FIG. 12. Upper row: left panel—azimuthal velocity profile and vorticity of the background barotropic double-eyewall cyclone with different heights of the walls. Right panel—Chebyshev grid points and thickness of the vortex $H(r)$. Lower row: radial structure $(u, v, \eta)(r)$ of the most unstable mode for the $l = 2$ on the left panel, and the corresponding pressure and velocity field on the right panel. Vertical lines indicate positions of the critical levels.

(directly related to the tangential momentum), as shown in Fig. 10. As in the case of single-eyewall vortex, the contribution of the mean in the dry case is almost inexistent, cf. Lahaye and Zeitlin,[11] while it is much more pronounced in the moist-convective case. At the stage of formation of the tripolar structure (middle panel), we observe a strong eddy flux in the outer regions of the vortex, which is responsible for the appearance of the cyclonic lobes. It is weaker in the moist-convective environment, compared to the dry one, and its impact is further diminished by the mean flux oriented in the opposite direction, while the latter is still negligible in the dry case. The mean flux in the moist-convective case is due to vorticity generation by moist convection, as explained by Lambaerts et al.[18] Nevertheless, the tripolar structure still forms in the moist-convective case, although its coherence is influenced by the weaker overall flux, as follows from its more diffused scatterplot in the right panel of Fig. 6. The picture is similar at the late stages (right panel), although the eddy flux in the moist-convective case becomes stronger than in the dry one, which helps to maintain the tripolar structure. Similar behavior is observed during the saturation of the unstable mode $l = 3$ (Fig. 8).

The details of formation of the end state are seen in Fig. 9, where we present the evolution of the individual azimuthal components of the azimuthal velocity. As follows from the figure, the $l = 3$ modes, initially following the exponential growth predicted by the linear stability analysis, saturate rather quickly, while the main contribution comes from the $l = 2$ mode with an admixture of the $l = 4$ mode. Modifications of the double-eyewall structure of the initial vortex due to evolving instability, as seen in the averaged azimuthal velocity, which is directly related to tangential momentum, and in potential vorticity, are tracked in Fig. 10. As follows from the right column of the figure, with both initializations, the inner eyewall, as seen in the azimuthal velocity field, is being smoothed down and gradually disappears (filling in the moat), while the outer wall wobbles around its initial position without much changes in the peak velocity. At the same time, the distribution of potential vorticity is being substantially smeared. We should stress that the peak azimuthal velocity in the moist-convective configuration is much stronger than in the dry one at the late stages of the evolution, as follows from Fig. 11, which illustrates the importance of the moist convection in the process.
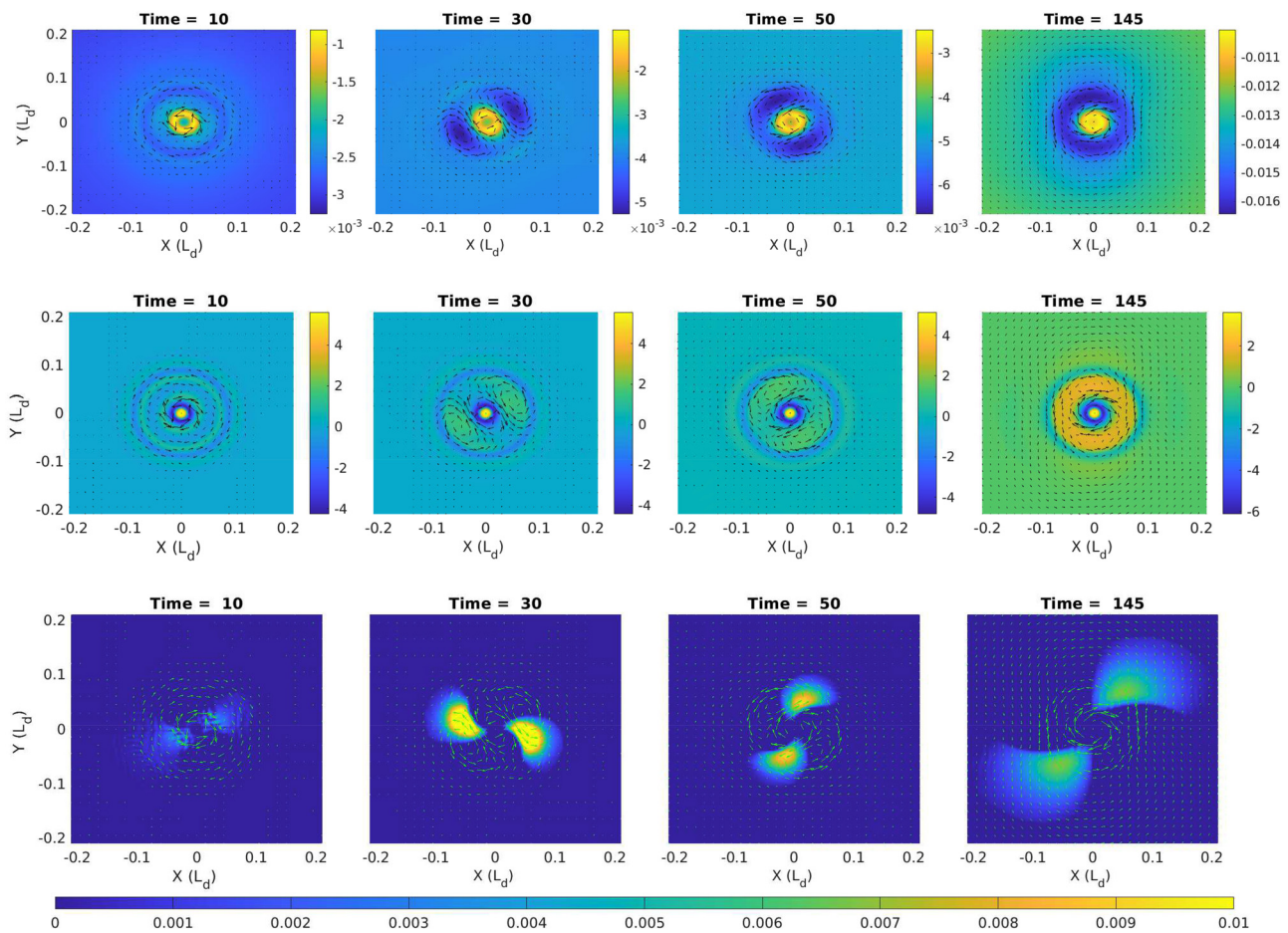

FIG. 13. Evolution of pressure anomaly (upper row), relative vorticity (middle row), and condensation (lower row) of double-eyewall cyclone in the moist-convective environment with initialization corresponding to Fig. 12.
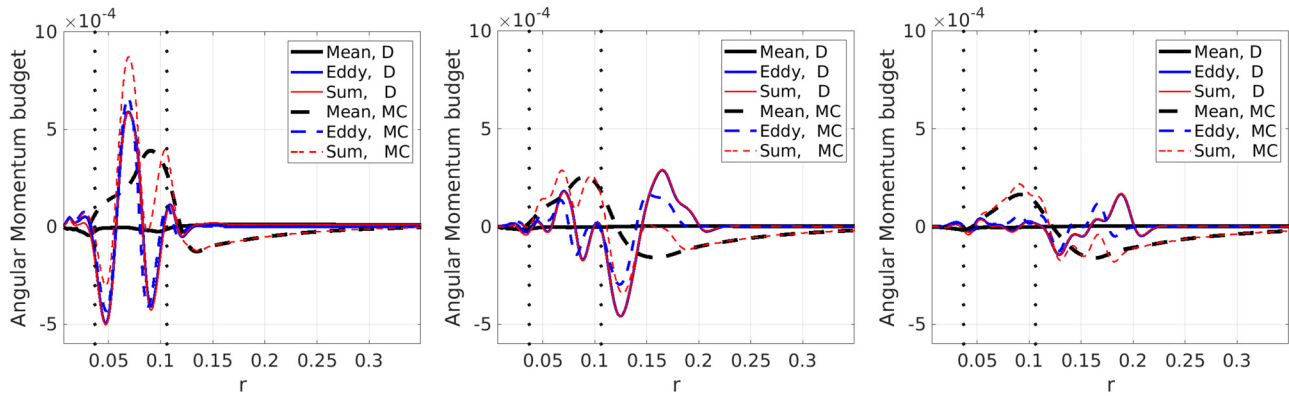
FIG. 14. Angular momentum budget integrated over three different time spans $\Delta t = [0, 50]$, $[51, 100]$, $[101, 145]$, and $[f_0^{-1}]$, from left to right, respectively, of eddy, mean, and sum fluxes of double-eyewall vortex with higher vorticity at the inner wall, as in Fig. 12, during nonlinear evolution of the most unstable mode, $l = 2$, in dry (solid) and moist-convective (dashed) environments. Vertical dots indicate the radial position of the radii of maximum winds of the inner and outer eyewalls at initial time.

IV. INSTABILITY OF DOUBLE-EYEWALL VORTEX WITH WEAKER OUTER WALL AND ITS NONLINEAR SATURATION

In this section, we briefly summarize the results of a similar investigation of the double-eyewall TC-like vortex with an outer wall of lesser intensity. They are presented in subsequent figures, which parallel the corresponding figures in Sec. III. For the sake of brevity, we present only the results of simulations initialized with the most unstable mode $l = 2$, as shown in Fig. 12. The overall result is that although the most unstable modes are similar, the evolution of the instability does not lead to a tripolar structure, but to a single-eyewall TC-like vortex, with the single wall produced by merging of initial inner and outer walls (Fig. 13). Notice a much lesser outward eddy fluxes in the angular momentum budget (Fig. 14) at the late stages, which is consistent with the absence of external vorticity lobes in this simulation.

V. CONCLUSIONS

We have shown that already the simplest shallow-water model with moist convection allows to capture some important features of the ERC. Our results indicate that disappearance of the inner eyewall is a purely dynamical effect of the developing barotropic instability. We have also shown that the enhancement of the secondary wall is due to the effects of moist convection. An unexpected result is the formation of coherent essentially tripolar structures as end states of double-eyewall TC-like vortices, which is observed in nonlinear saturation of the barotropic instability in the case of eyewalls of comparable intensity. This process is not much influenced by the diabatic processes. The resulting end states have a much more complicated structure than tripolar vortices studied previously in the framework of 2D Euler and rotating shallow water systems and in laboratory experiments. The central vortex of these states, although being practically axisymmetric, has a complex form with alternating annuli of anticyclonic and cyclonic vorticity. Such structures are interesting by themselves from a purely hydrodynamical viewpoint and merit further investigation. We are not aware of observational evidence of such structures, but their robust emergence in our simulations invites for a closer look into the data.
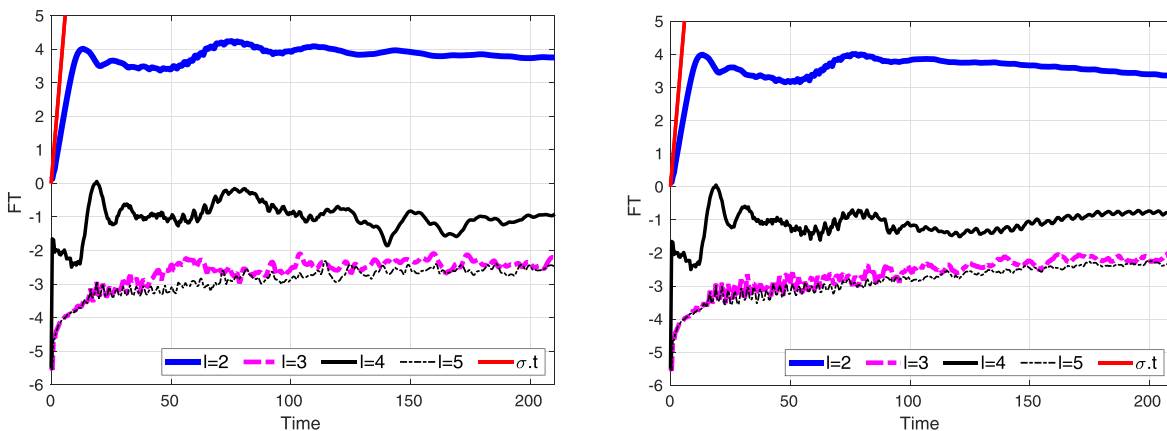

FIG. 15. Logarithms of the normalized amplitudes of the Fourier modes of azimuthal velocity as functions of time during the evolution of the barotropic instability in adiabatic (left) and moist-convective (right) environments. σ represents the linear growth rate. Initial conditions as in Fig. 12.

Our simulations also show a high sensibility of the evolution scenario to fine details of the double-wall vortex structure, especially to the relative height of the walls, which hints at difficulties in forecasting the evolution of double-eye hurricanes.

ACKNOWLEDGMENTS

AUTHOR DECLARATIONS
Conflict of Interest

The authors have no conflicts to disclose.

Author Contributions

Masoud Rostami: Conceptualization (equal); formal analysis (equal); funding acquisition (equal); investigation (equal); methodology (equal); resources (equal); software (equal); validation (equal); visualization (equal); writing – original draft (equal); writing – review & editing (equal). **Vladimir Zeitlin:** Conceptualization (equal); formal analysis (equal); investigation (equal); methodology (equal); project administration (equal); supervision (equal); validation (equal); visualization (equal); writing – original draft (equal); writing – review & editing (equal).

DATA AVAILABILITY

The data that support the findings of this study are available from the corresponding author upon reasonable request.

REFERENCES

[1]H. E. Willoughby, J. A. Clos, and M. G. Shoreibah, "Concentric eye walls, secondary wind maxima, and the evolution of the hurricane vortex," J. Atmos. Sci. **39**, 395–411 (1982).

[2]H. E. Willoughby, "The dynamics of the tropical cyclone core," Aust. Meteorol. Mag. **36**, 183–191 (1988).

[3]J. D. Hawkins, M. Helveston, T. F. Lee, F. J. Turk, K. Richardson, C. Sampson, J. Kent, and R. Wade, "Tropical cyclone multiple eyewall configurations," in *Extended Abstracts, 27th Conference on Hurricanes and Tropical Meteorology, Monterey, CA* (American Meteorological Society, 2006).

[4]J. P. Kossin and M. Sitkowski, "An objective model for identifying secondary eyewall formation in hurricanes," Mon. Weather Rev. **137**, 876–892 (2009).

[5]C. E. Samsury and E. J. Zipser, "Secondary wind maxima in hurricanes: Airflow and relationship to rainbands," Mon. Weather Rev. **123**, 3502–3517 (1995).

[6]M. L. Black and H. E. Willoughby, "The concentric eyewall cycle of hurricane Gilbert," Mon. Weather Rev. **120**, 947–957 (1992).

[7]J. Molinari, J. A. Zhang, R. F. Rogers, and D. Vollaro, "Repeated eyewall replacement cycles in hurricane Frances (2004)," Mon. Weather Rev. **147**, 2009–2022 (2019).

[8]L. J. Shapiro and H. E. Willoughby, "The response of balanced hurricanes to local sources of heat and momentum," J. Atmos. Sci. **39**, 378–394 (1982).

[9]A. G. Pendergrass and H. E. Willoughby, "Diabatically induced secondary flows in tropical cyclones. Part I: Quasi-steady forcing," Mon. Weather Rev. **137**, 805–821 (2009).

[10]M. Sitkowski, J. P. Kossin, and C. M. Rozoff, "Intensity and structure changes during hurricane eyewall replacement cycles," Mon. Weather Rev. **139**, 3829–3847 (2011).

[11]N. Lahaye and V. Zeitlin, "Understanding instabilities of tropical cyclones and their evolution with a moist convective rotating shallow-water model," J. Atmos. Sci. **73**, 505–523 (2016).

[12]W. H. Schubert, C. J. Slocum, and R. K. Taft, "Forced, balanced model of tropical cyclone intensification," J. Met. Soc. Jpn. Ser. II **94**, 119–135 (2016).

[13]M. Rostami and V. Zeitlin, "An improved moist-convective rotating shallow-water model and its application to instabilities of hurricane-like vortices," Q. J. R. Met. Soc. **144**, 1450–1462 (2018).

[14]D. A. Schecter, "Distinct intensification pathways for a shallow-water vortex subjected to asymmetric 'diabatic' forcing," Dyn. Atmos. Oceans **91**, 101156 (2020).

[15]M. Rostami and V. Zeitlin, "Evolution, propagation and interactions with topography of hurricane-like vortices in a moist-convective rotating shallow-water model," J. Fluid Mech. **902**, A24 (2020).

[16]T.-K. Lai, E. A. Hendricks, and M. K. Yau, "Long-term effect of barotropic instability across the moat in double-eyewall tropical cyclone-like vortices in forced and unforced shallow-water models," J. Atmos. Sci. **78**, 4103–4126 (2021).

[17]F. Bouchut, J. Lambaerts, G. Lapeyre, and V. Zeitlin, "Fronts and nonlinear waves in a simplified shallow-water model of the atmosphere with moisture and convection," Phys. Fluids **21**, 116604 (2009).

[18]J. Lambaerts, G. Lapeyre, and V. Zeitlin, "Moist versus dry barotropic instability in a shallow-water model of the atmosphere with moist convection," J. Atmos. Sci. **68**, 1234–1252 (2011).

[19]M. Rostami and V. Zeitlin, "Influence of condensation and latent heat release upon barotropic and baroclinic instabilities of vortices in a rotating shallow water f-plane model," Geophys. Astrophys. Fluid Dyn. **111**, 1–31 (2017).

[20]K. Katsaros, "Evaporation and humidity," in *Encyclopedia of Ocean Sciences*, edited by John H. Steele (Academic Press, Oxford, 2001), pp. 870–877.

[21]T. W. Cronin and D. R. Chavas, "Dry and semidry tropical cyclones," J. Atmos. Sci. **76**, 2193–2212 (2019).

[22]K. J. Mallen, M. T. Montgomery, and B. Wang, "Reexamining the near-core radial structure of the tropical cyclone primary circulation: Implications for vortex resiliency," J. Atmos. Sci. **62**, 408–425 (2005).

[23]N. Lahaye and V. Zeitlin, "Collisions of ageostrophic modons and formation of new types of coherent structures in rotating shallow water model," Phys. Fluids **23**, 061703 (2011).

[24]M. Rostami and V. Zeitlin, "Eastward-moving convection-enhanced modons in shallow water in the equatorial tangent plane," Phys. Fluids **31**, 021701 (2019).

[25]M. Rostami and V. Zeitlin, "Eastward-moving equatorial modons in moist-convective shallow-water models," Geophys. Astrophys. Fluid Dyn. **115**, 345–367 (2021).

[26]L. Polvani and X. Carton, "The tripole: A new coherent structure of incompressible two-dimensional flow," Geophys. Astrophys. Fluid Dyn. **51**, 87 (1990).

[27]R. R. Trieling, G. G. F. vanHejst, and Z. Kizner, "Laboratory experiments on multipolar vortices in rotating fluid," Phys. Fluids **22**, 094104 (2010).

[28]E. A. Hendricks, W. H. Schubert, Y.-H. Chen, H.-C. Kuo, and M. S. Peng, "Hurricane eyewall evolution in a forced shallow-water model," J. Atmos. Sci. **71**, 1623–1643 (2014).